Supplementary Information

Monodispersed SnS nanoparticles anchored on carbon nanotubes for high-retention sodium-ion batteries

Thi Hoai Thuong Luu[a,b], Dinh Loc Duong[a,b], Tae Hoon Lee[c], Duy Tho Pham[d], Ramkrishna Sahoo[e], Gyeongtak Han[b], Young-Min Kim[a,b] and Young Hee Lee[a,b]*

[a]Center for Integrated Nanostructure Physics (CINAP), Institute for Basic Science (IBS), Suwon 16419, Republic of Korea.

[b]Department of Energy Science, Sungkyunkwan University (SKKU), Suwon 16419, Republic of Korea.

[c]Photo Equipment group, SEMES Co. Ltd., 77 4sandan 5-gil, Seobuk-gu, Cheonan 31040, Republic of Korea.

[d]Department of Chemical Engineering, Pohang University of Science and Technology (POSTECH), 77 Cheongnam-Ro, Nam-Gu, Pohang, 37673, Republic of Korea.

[e]Centre for Advanced Studies (CAS), Dr. APJ Abdul Kalam Technical University (AKTU), Lucknow, India.

*Corresponding author

E-mail address: leeyoung@skku.edu (Y. H. Lee)

Density functional calculation method

Density functional calculation (DFT) was performed using DMOL3 code. The exchangecorrelation was estimated by the generalized gradient approximation with the Perdew-BurkeErnzerh functional. The double-numeric quality basis set with polarization functions was used with a cut-off radius of 4.9 Å . The (4,4) carbon nanotube (CNT) with a length of 14.76 Å terminated by H at two ends was investigated. All structures were optimized to reach the energy convergence of 10^{-5} Ha. The binding energy (E_b) of SnS on CNT was calculated by the equation: $E_b = E_{CNT-SnS} - E_{CNT} - E_{SnS}$; where $E_{CNT-SnS}$, E_{CNT}, E_{SnS} are the energies of SnS on CNT system, pristine CNT, and SnS molecule, respectively.

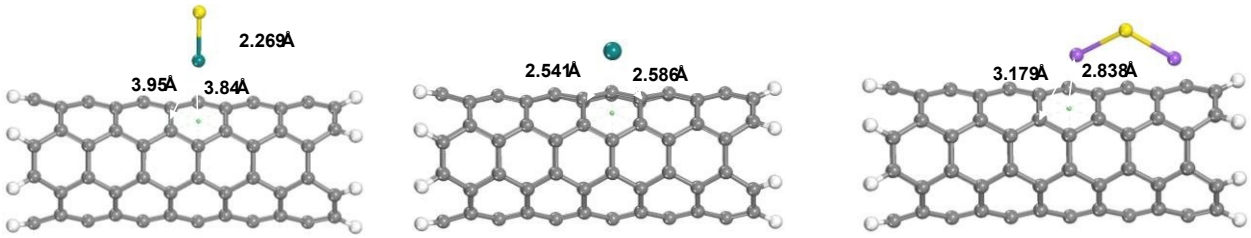

Figure D1. DFT calculation of interaction between SnS, Sn and Na_2S with the CNT, respectively (a -c). The Carbon atoms, Tin atoms, sulfur atoms and sodium atoms are grey, cyan, yellow and violet, respectively.

The DFT calculations were performed to gain the cohesive energy between SnS-CNT moieties (Fig. D1). The binding energy of SnS-CNT is -0.46eV that represents the exothermic reaction. As assumed elsewhere, the weaker binding energy between the tin sulfide and the conducting agent can trigger the dissociation of the metal sulfide from conducting network during the cycling test, then lead to the aggregation of SnS nanoparticles and volume expansion [1]. Compared to the previous calculation between SnS and graphene (near 0), the SnS-CNT bonding shows higher cohesive binding energy [1]. Moreover, SnS sodiation products, Sn and Na_2S, can further robustly anchor on the CNT network as confirmed by the calculated DFT data. The cohesive energy of SnCNT is -1.4eV while Na_2S-CNT even shows higher binding energy with the value of -2.8 eV, these can make the desodiation proceed more efficiently. The strong cohesive bindings can help the structure more stable then be favorable for long-cycles stability during the battery operation.

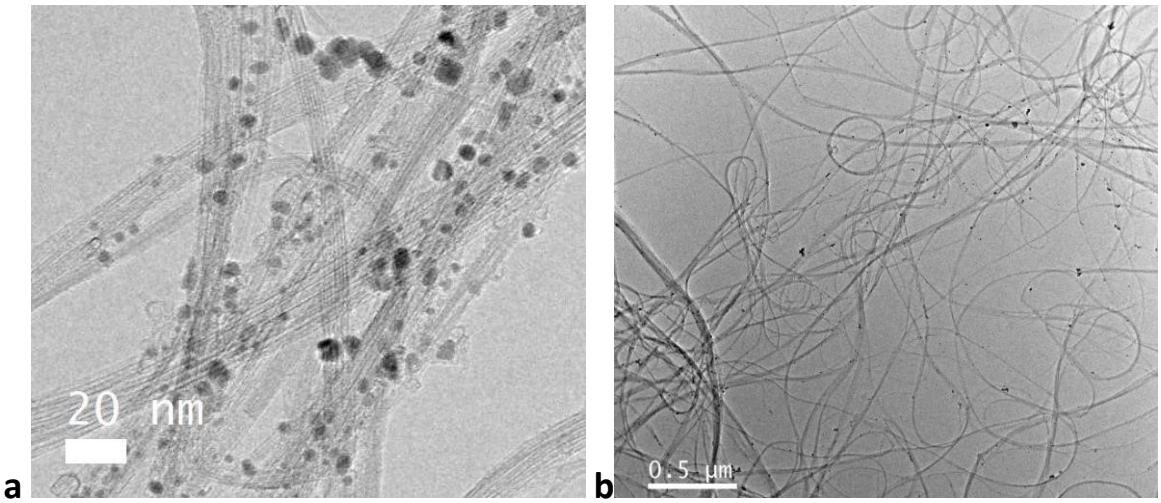

Figure S1: TEM images of CNTs after mild oxidation.

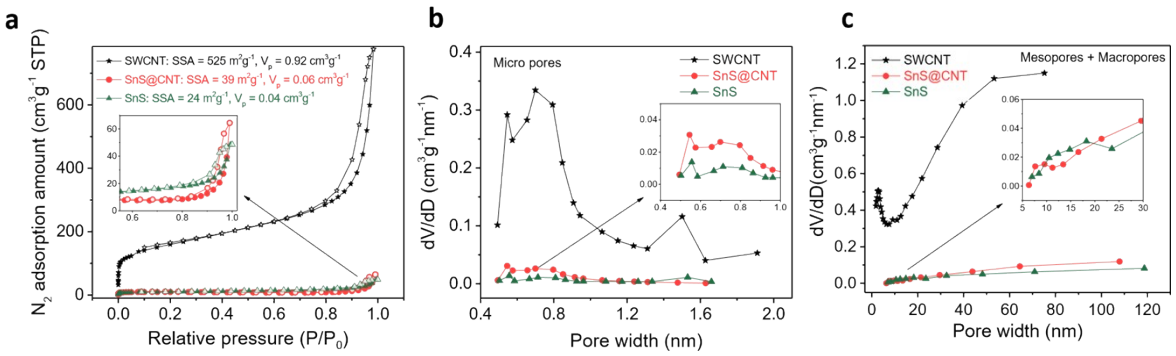

Figure S2. Brunauer–Emmet–Teller (BET) data for Single wall carbon nanotube (SWCNT), SnS nanoparticles anchored on carbon nanotubes (SnS@CNT) and SnS nanoparticles (SnS): (a) N_2 adsorption/desorption isotherms, (b) micropore distribution, and (c) macropore and mesopore distribution. Here BET SSA is the BET specific surface area and dV/dD is the differential pore volume vs. diameter.

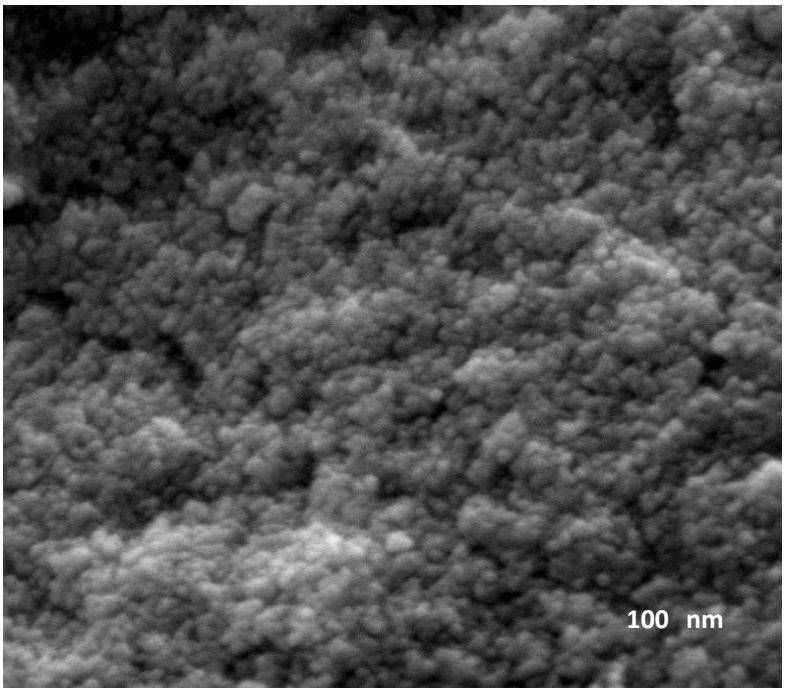

Figure S3: SEM image of SnS nanoparticles**.**

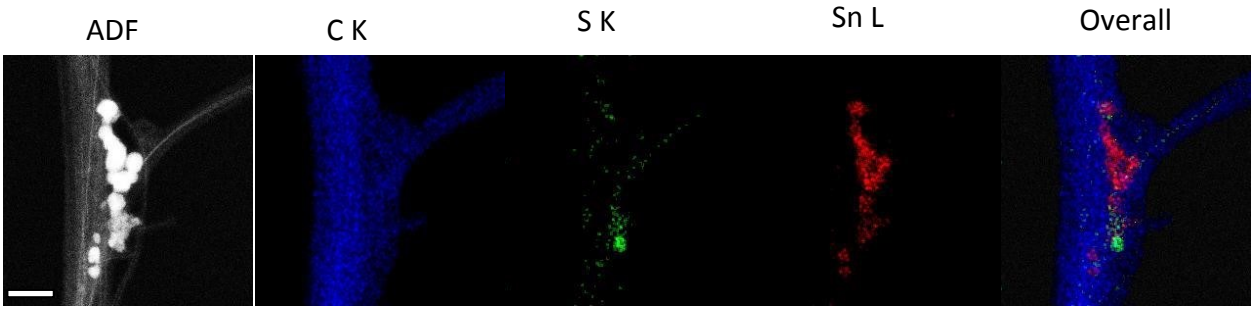

Figure S4: TEM EDS mapping data of SnS@CNT sample. Carbon, sulfur and tin are in blue, sulfur and red, respectively.

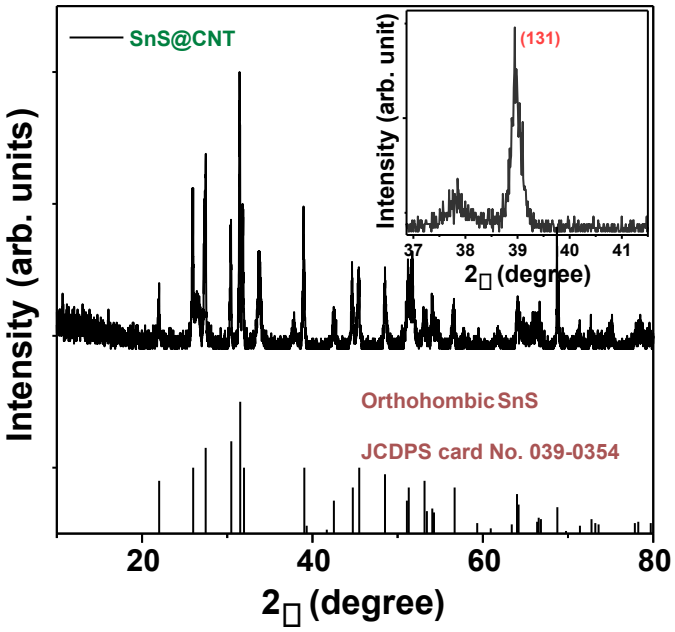

Figure S5. X-ray diffraction (XRD) spectrum of SnS_2 nanoparticles anchored on carbon nanotubes (SnS_2@CNT) annealed at 625 °C and archived XRD spectrum for orthorhombic SnS (JCPDS Card No. 039-0354). The inset picture is the magnified image of the peak at 39.05° (131), which was used to extract the full width at half maximum data to calculate the particle size.

The size of the nanoparticles was calculated using the Scherer equation utilizing X-ray diffraction (XRD) data: $D = K\lambda/(\beta \cos\theta)$, where D is the mean size of crystallites (nm), K is the crystallite shape factor or Scherrer constant, which is approximately 0.9 for spherical particles, λ is the Xray wavelength (nm) (λ = 1.5406 nm for Cu $K_{\alpha 1}$), β is the full width at half maximum (FWHM) of the XRD peak (rad), and Θ is the Braggs angle (°) [2][3]. Here, we used the 2θ peak of 39.05° (inset graph in Fig. S3) and calculate the FWHM to be 0.288 rad. The calculations indicated that the diameter of the particles was 5.11 nm, which was a reasonable match to the value estimated using the transmission electron microscopy image.

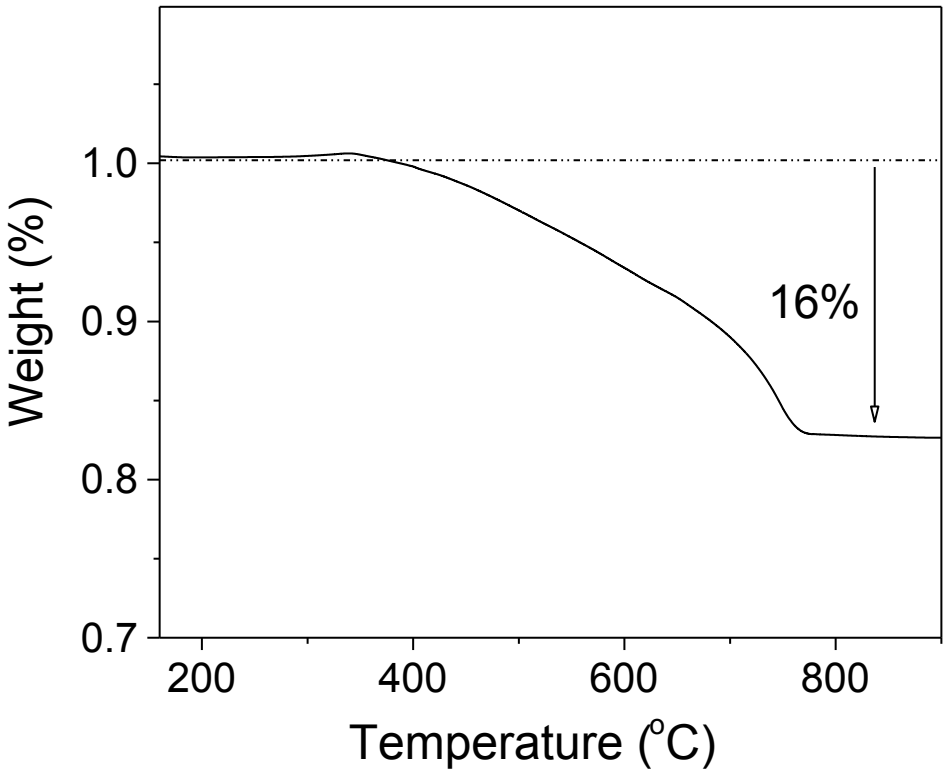

Figure S6. Thermogravimetric analysis data of SnS nanoparticles anchored on carbon nanotubes in air.

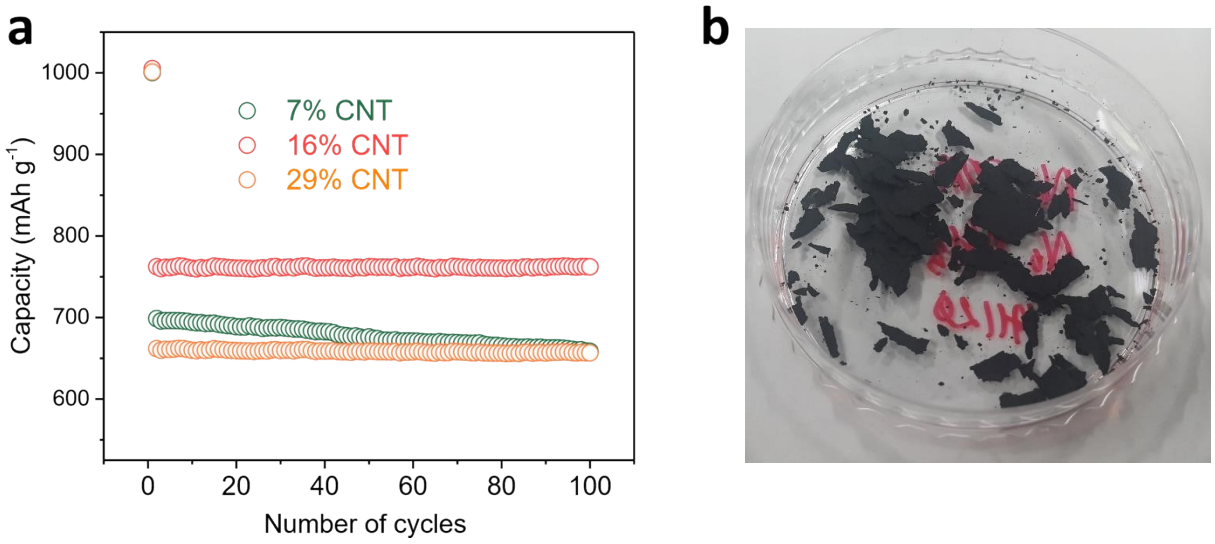

Figure S7: (a) Discharge values of SnS@CNT sample with different CNTs content during 100 cycles at current density of 100 mA g^{-1}; (b) the condition of SnS@CNT with 7% CNT after peeled off from filtered paper.

The ratio of SnS@CNT in the paper was optimized to show achieve the excellent capacity and good stability. We compared discharge value of different SnS@CNT samples with varied CNT contents, 7%, 16%, 29% which were noted as SnS@CNT7, SnS@CNT16, SnS@CNT29, respectively at s current density of 100 mA g^{-1} as depicted in figure S7 above. One note to make here is, the 7% content of CNT was not sufficient to form the thin film as figure S7b due to the small CNT content, and thus additional carbon black was necessary with SnS@CNT7 slurry with the weight ratio SnS : carbon black : PVDF = 85 : 5 : 10. At a few cycles, because the usage of binder and conducting polymer, then SnS@CNT7 sample showed the capacity similar with SnS@CNT16. However, the stability is poor and the retention was decreased significantly after 100 cycles due to the existence of the PVDF. At high CNT content (29%), no significant change in the capacity was found to SnS@CNT16. Therefore, SnS@CNT16 was chosen to ensure the stability and high capacity.

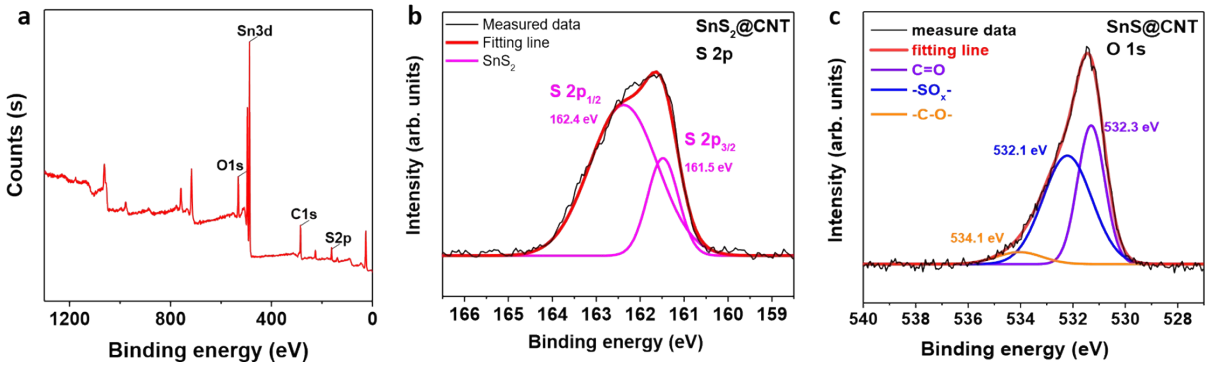

Figure S8. (a) Survey X-ray photoelectron spectroscopy (XPS) profiles of SnS nanoparticles anchored on carbon nanotubes (SnS@CNT); (b) S 2p XPS data of SnS_2 nanoparticles anchored on carbon nanotubes (SnS_2@CNT); (c) high resolution O 1s XPS profile of SnS@CNT.

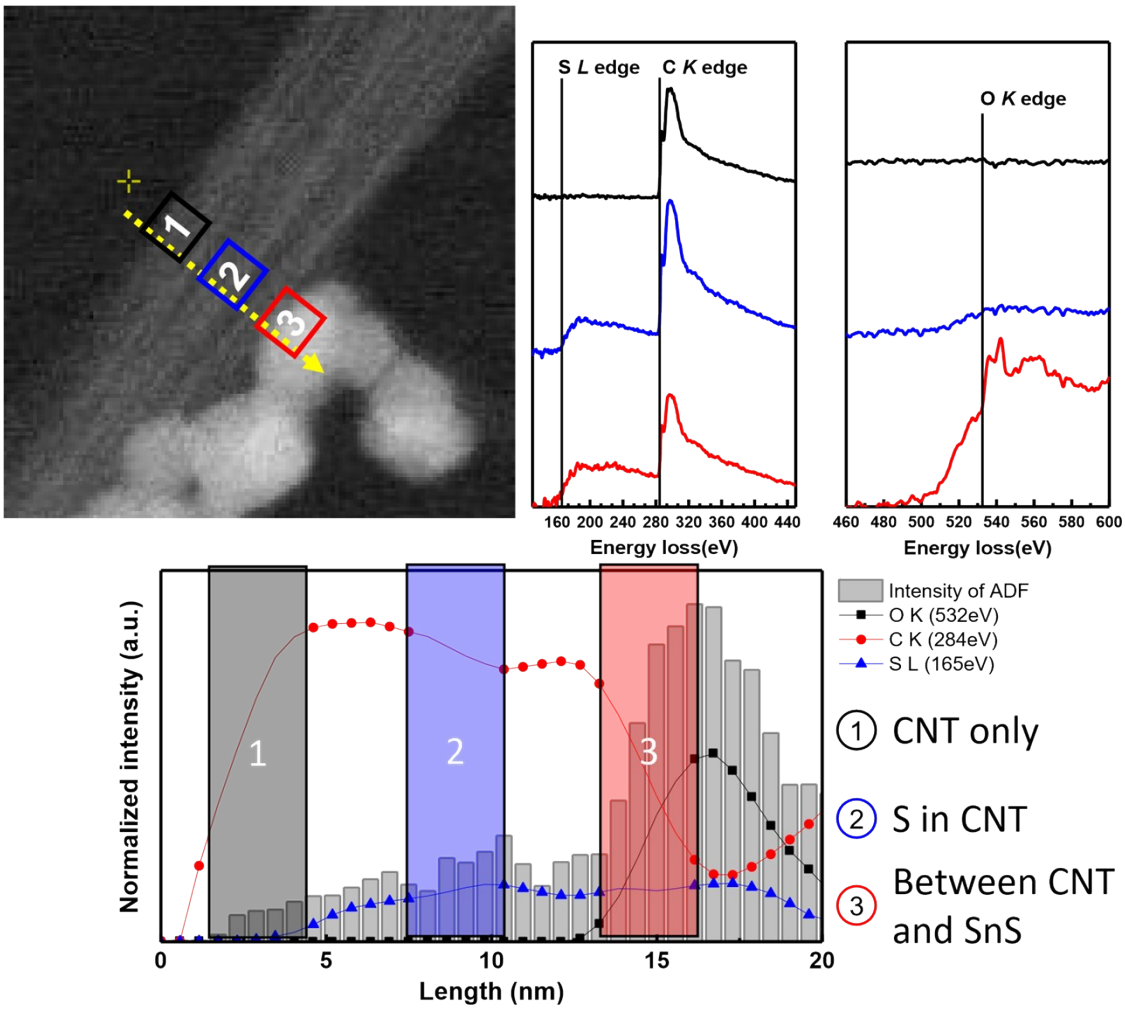

Figure S9: Electron energy loss near-edge structure (ELNES) of SnS@CNT.

To further confirm oxygen impurities, here we performed electron energy loss spectrum. As depicted in TEM image in Fig. 1d in the main manuscript, SnS nanoparticles are anchored on the CNT strands. The data of electron energy loss near-edge structure (ELNES) of S L, C K and O K edges was presented here in new Fig. S9 above. We scanned the sample into 3 areas as denoted in the TEM image: zone 1 is pure CNT, zone 2 is S-doped CNT and zone 3 is SnS anchored near the CNT strand. In zone 1, pure CNT was identified with C K edge. The existence of sulfur in zone 2 is confirmed through S L edge with a signature of oxygen from O K edge. In zone 3, there was an increase in intensity for S L edge due to the presence of SnS nanoparticles in addition to rich O K edge due to oxygen atoms accumulated on the CNT surface during acid treatment. S L edge peaks are broad due to the presence of oxygen bonds. This implies strong bond between oxygen atom and SnS nanoparticles.

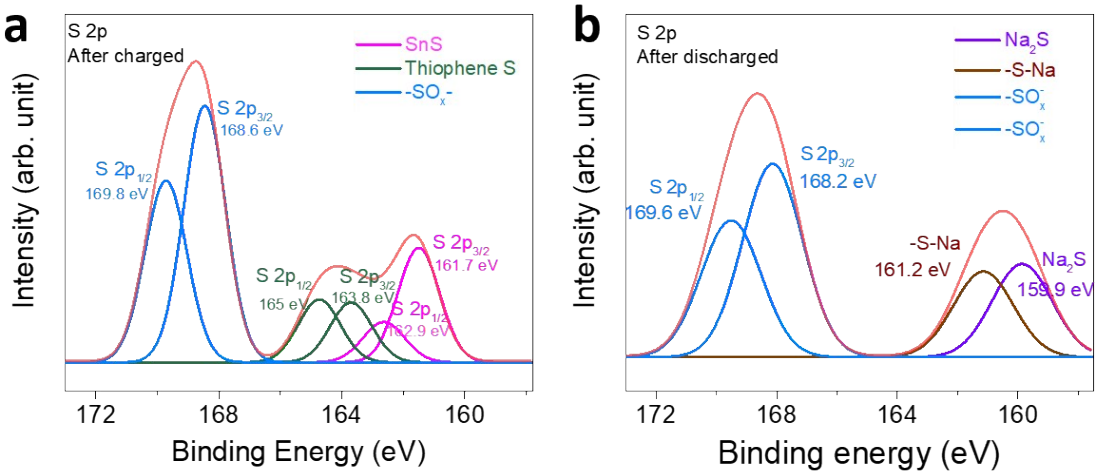

Figure S10: S 2p X-ray photoelectron spectroscopy (XPS) profiles of SnS@CNT: (a) after charged, (b) after discharged at a current density of 0.1 A g^{-1}.

We measured ex-situ XPS of SnS@CNT after 100 cycles at a current density of 0.1 A g^{-1} (charged state and discharged state). The sulfur binding energy was presented in new figure S10 above. In the charged state or desodiation process, we observed the binding energies from metal sulfur, thiophene ring and sulfonate or sulfate bonding but the binding energy peaks were a little shifted compared to the pured SnS@CNT in figure 3c in the revised main manuscript. For the discharged state or sodiation, sodium sulfide was formed after sodiation; NaS_2. Interestingly, the sulfur reacted to sodium during the sodiation process and therefore the peak of –S-Na appeared in the XPS data.

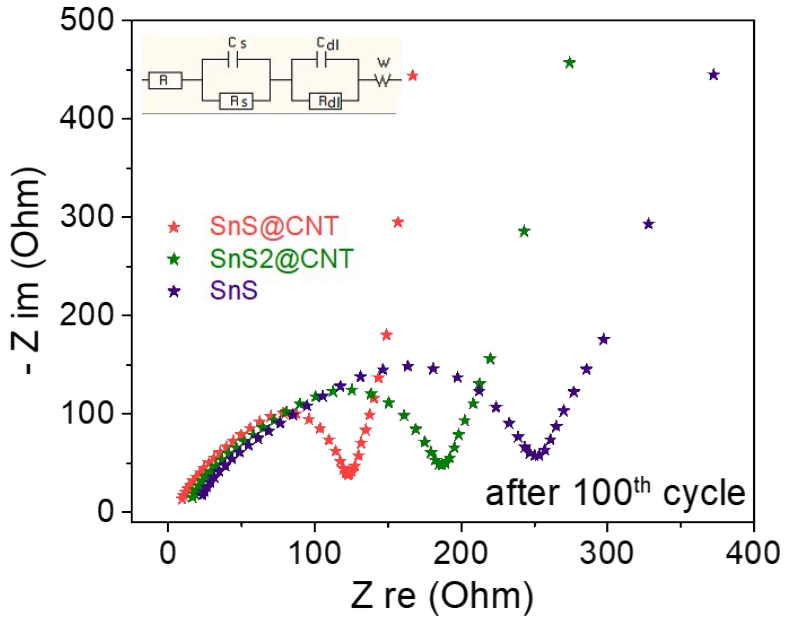

Figure S11: EIS spectra of SnS@CNT, SnS_2@CNT and SnS nanoparticle after 100 cycles.

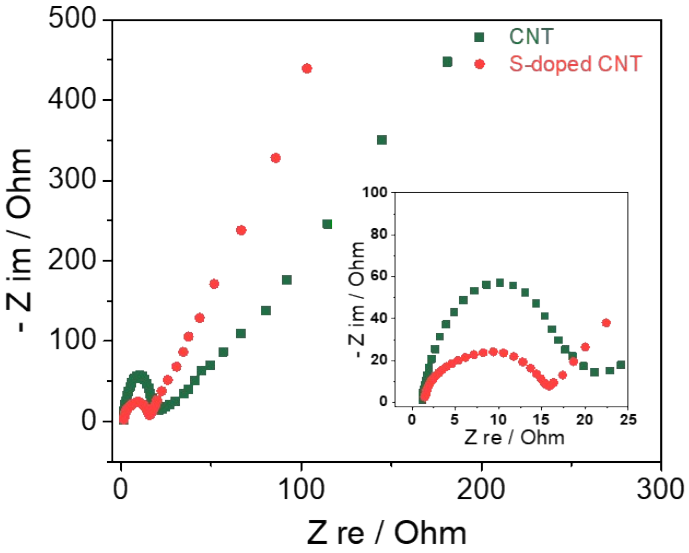

Figure S12: EIS spectra of pure CNT and S-doped CNT.

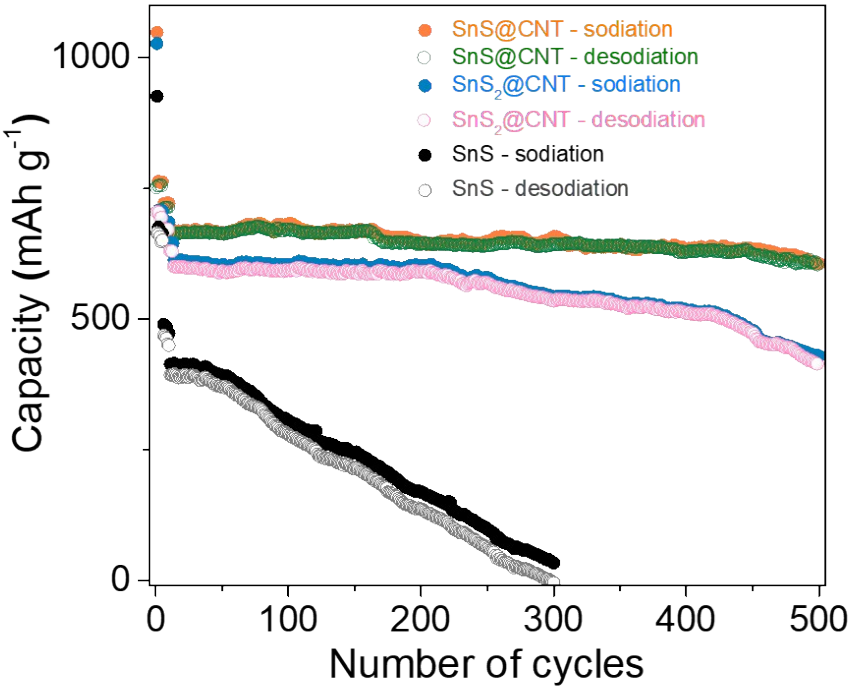

Figure S13. Stability of SnS nanoparticles, SnS_2 nanoparticles anchored on carbon nanotubes (SnS_2@CNT) and SnS nanoparticles anchored on carbon nanotubes (SnS@CNT) at the current of 1 A g^{-1}.

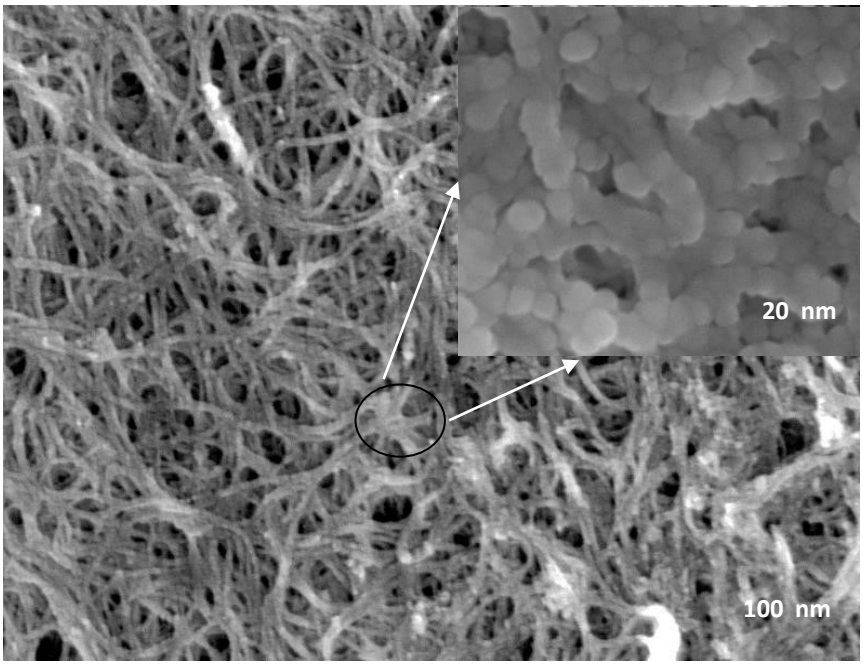

Figure S14: SEM image of SnS@CNT after 700 cycles at a current density of 1 A g^{-1}. The inset is the magnified sample surface.

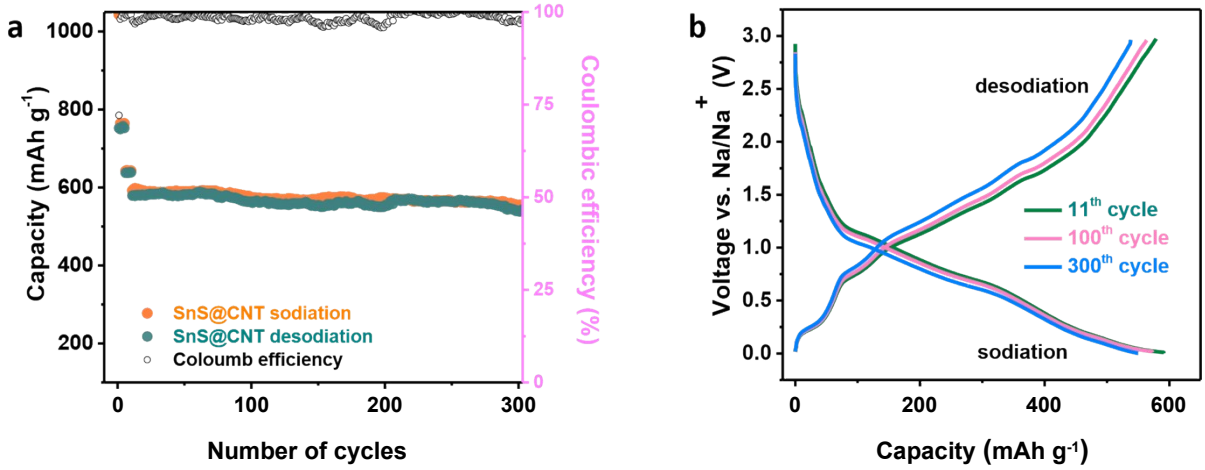

Figure S15. (a) Cycle stability of SnS nanoparticles anchored on carbon nanotubes (SnS@CNT) at the current of 2 A g^{-1}. (b) Discharge/Charge profiles of SnS@CNT at 2 A g^{-1} after different number of cycles.

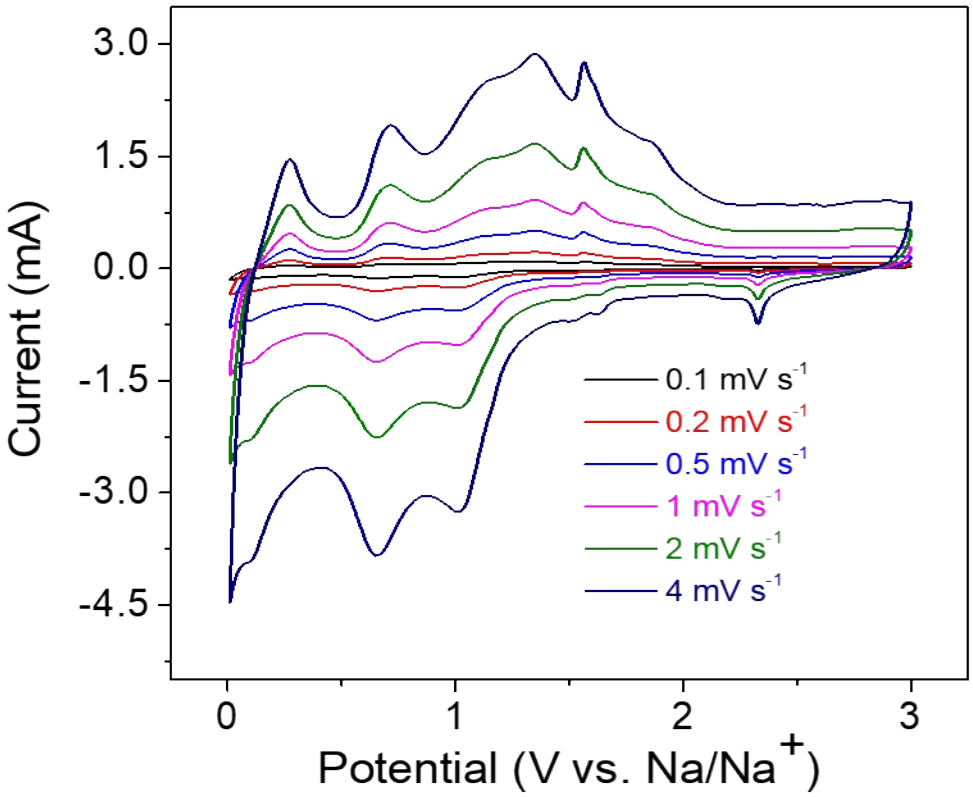

Figure S16. Cyclic voltammetry curves of SnS nanoparticles anchored on carbon nanotubes at different scan rates.

Table S1. Capacity and retention values of different anode materials reported in the literature compared with the anode material used in this study.

Material	**Capacity (mAh g^{-1})**	**Retention (%)**	**Ref**
SnS NPs/CNT	210 (at 0.5 A g^{-1} after 100 cycles)		[4]
SnS-C	548 (at 0.1 A g^{-1} after 100 cycles)	94	[5]
SnS/CNTs@S-CNFs	296 (at 0.8 A g^{-1} after 600 cycles)	78.9	[6]
3D SnS/C	535 (at 1 A g^{-1} after 300 cycles)	80	[7]
SnS/CNT	450 (at 0.2 A g^{-1} after 100 cycles)	71	[8]
C@SnS/SnO_2@Gr	409 (at 810 mA g^{-1} after 500 cycles)	73	[9]
C-coated SnS nanotubes	440.4 (at 0.2 A g^{-1} after 100 cycles)	96	[10]
SnS_2/NGS	453 (at 0.1 A g^{-1} after 200 cycles)	87.4	[11]
SnS hollow nanofibers	289 (at 1A g^{-1} after 500 cycles)	93	[12]
SnS nanosheets on CMT	460 (at 0.1 A g^{-1} after 500 cycles)	88.7	[13]
SnS@CNT	**615 (at 1 A g^{-1} after 500 cycles)**	**92**	**This study**

Extraction of sodium ion diffusion coefficient from CV profiles

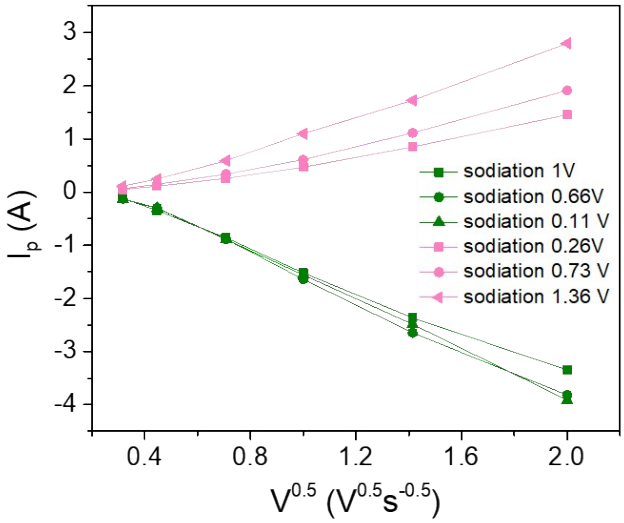

Figure S17: Graph of normalized peak current vs square root of the scan rate at different cathodic and anodic voltages extracted from Fig. S16.

The diffusion equation can be expressed through the relationship between peak current (I_p), voltage scan rate and diffusion constant (D) [14], as below:

$I_p/m = 0.4463\ F\ (F/RT)^{0.5} C_i V^{0.5} A D^{0.5}$ (*)

Where I_p: peak current in amperes, m: mass of the electrode, F: Faraday constant, R: Boltzmann constant, T: absolute temperature, C_i: initial concentration of metal ion in mol cm^{-3} (C_i is taken as the total amount of Na in a particle before desodiation), V: scan rate in Vs^{-1}, A: electrode area in cm^2 (BET data), D: diffusion constant in cm^2s^{-1}.

Figure S17 is plot of I_p as a square root of the scan rat ($V^{0.5}$) of anode material which give the slope data of equation (*) to calculate the diffusion constants (cathodic diffusion (D), anodic (D)) as Table 1 below,

SnS@CNT	**Sodiation peak**			**Desodiation peak**		
$D_{Na+}(cm2s-1)$	0.11 V	0.66 V	1 V	0.26 V	0.73 V	1.36 V
	5.43×10^{-12}	7.23×10^{-12}	7.3×10^{-12}	9.98×10^{-13}	1.71×10^{-12}	3.63×10^{-12}

Table 2: Calculated D_{Na^+} of SnS@CNT from voltage scan rates at room temperature.

REFERENCES

1. X. Xiong, C. Yang, G. Wang, Y. Lin, X. Ou, J. Wang, B. Zhao, M. Liu, Z. Lin Z. and K. Huang, *Energy Environ. Sci.*, 2017, **10**, no. 8, pp. 1757–1763.
2. A. Monshi, M. R. Foroughi and M. R. Monshi, *World J. Nano Sci. Eng.*, 2012, **02**, pp. 154– 160.
3. D. M. Smilgies, *J. Appl. Crystallogr.*, 2009, **42**, no. 6, pp. 1030–1034.
4. Y. Chen, B. Wang, T. Hou, X. Hu, X. Li, X. Sun, S. Cai, H. Ji and C. Zheng, *Chinese Chemicals Letters*, 2018, **29**, pp. 187–190.
5. L. Wu, H. Liu, L. Xiao, J. Qian, X. Ai, H. Yang H and Y. Cao, *Journal of Materials Chemistry A*, 2014, **2,** pp. 16424–16428.
6. S. Zhang, H. Zhao, M. Wang, Z. Li and J. Mi, *Electrochimica Acta*, 2018, **279**, pp. 186–194.
7. C. Zhu, P. Kopold, W. Li, P. A. van Aken, J. Maier and Y. Yu, *Adv. Sci.*, 2015, **2**, pp. 1–8.
8. S. Zhang, L. Yue, H. Zhao, Z. Wang and J. Mi, *Materials Letters,*, 2017, **209**, pp. 212–215.
9. Y. Zheng, T. Zhou, C. Zhang, J. Mao, H. Liu and Z. Guo, *Angew. Chemie - Int. Ed.*, 2016, **55**, pp. 3408–3413.
10. P. He, Y. Fang, X. Y. Yu and X. W. D Lou, *Angew. Chemie - Int. Ed.*, 2017, **56**, pp. 12202–

    12205. 11. S. Tao. D. Wu, S. Chen, B. Qian, W. Chu and L. Song, *Chem. Commun.*, 2018, **54**, pp.

    8379–8382.
12. H. Jia, M. Dirican, N. Sun, C. Chen, P. Zhu, C Yan, X. Dong, Z. Du, J. Guo, Y. Karaduman, J. Wang, F. Tang, J. Tao and X. Zhang, *Chem. Commun.*, 2019, **55**, pp. 505–508.
13. J. Zhao, G. Wang, R. Hu, K. Zhu, K. Cheng, K. Ye, D. Cao and Z. Fan, *J. Mater. Chem. A*, 2019, **7**, pp. 4047–4054.
14. D. Y. W. Yu, C. Fietzek, W. Weydanz, K. Donoue, T. Inoue, H. Kurokawa and S. Fujitani, *J. Electrochem. Soc.,* 2007, **154**, 4, A253-A257.